Large optical conductivity of Fermi arc states in Weyl and Dirac semimetal nanowires

Wenye Duan [●],[1,*] XiangDong Lu [●],[1] and Jun-Feng Liu[2]

[1]*School of Physics, East China University of Science and Technology, Shanghai 200237, China*
[2]*School of Physics and Materials Science, Guangzhou University, Guangzhou 510006, China*

We theoretically study the band structure and optical conductivity in the Weyl and Dirac semimetal nanowires. It is found that the Fermi arc states play a crucial role in the optical conductivity. The optical conductivity shows an anisotropic dependence on the optical polarization axis. The qualitative anisotropy is attributed to the underlying band structure and distinct optical selection rules. For an optical polarization axis parallel to the nanowire, the optical resonant transitions are between Fermi arc and bulk states or bulk and bulk states. On the other hand, when the polarization axis is perpendicular to the nanowire, there are additional transitions between Fermi arc and Fermi arc states aside from the transitions aforementioned. They contribute to a giant resonant peak. The amplitude of this ultrastrong resonant peak is 10 times stronger than other responses. Moreover, these characteristic features of optical conductivities can be observed even with a finite chemical potential which is out of the bulk gap and are robust to disorders. In a word, the large resonant peak due to Fermi arc states and strong anisotropy of optical conductivities provide an optical means to probe the dynamics of the Fermi arc states in Weyl and Dirac semimetal nanowires. We hope that our study could give a valuable theoretical reference for nanoelectronics and ultrafast optoelectronic applications based on nanowires of Dirac and Weyl materials.

I. INTRODUCTION

Weyl and Dirac semimetals have attracted a tremendous amount attention recently as the famous examples of topological semimetals [1,2]. They are characterized by the gapless bulk twofold Weyl or fourfold Dirac nodes protected by topology and/or symmetry. The corresponding low-energy bulk excitations are the Weyl and Dirac fermions as analogs of particles in high-energy physics. One of their distinct signatures is the Fermi arc surface states which are protected by the topology of the bulk band structure and link the projections on the surface Brillouin zone of the different bulk nodes. The Fermi arc surface states were experimentally observed in various materials by means of surface probe techniques (such as angle-resolved photoemission spectroscopy, scanning tunneling microscopy, scanning tunneling spectroscopy, and the quasiparticle interference patterns) [2–4]. The exotic transport properties of the Weyl and Dirac semimetals, due to their characteristic electronic properties in the bulk states, have been intensively studied both theoretically and experimentally [1,2]. On the other hand, several works investigated the contributions of the Fermi arc states in finite-size devices to the band structure and the transport phenomena both theoretically and experimentally [5–41], such as nonlocal transports [5,6], quantum oscillations [28–33], and three-dimensional (3D) quantum Hall effect [35–41]. The influences of phonon-induced backscattering on transport have also been investigated for both the slab geometry [23,42] and nanowires [24]. Particularly, it was shown that the

contribution of Fermi arc states to the conductance is salient and crucial at low energy in nanowires of Weyl and Dirac semimetals [22,26,27]. It is found two distinct regimes for the conductance depending on the chemical potential: "surface regime" and "bulk-surface regime" [22,26,27]. In order to probe the conductance conditioned by only Fermi arc states, the chemical potential should be adapted low enough to be in the bulk confinement gap where only the Fermi arc states exist. Experimentally, the nanowires of Weyl and Dirac semimetals are realizable recently [15–21,25,43].

Optical conductivity can reveal valuable information on the charge dynamics, which is hard to obtain in DC measurements. It can be used to detect the underlying band structures and to design optoelectronic devices. The optical [44–48] and magneto-optical conductivities [44,49] have been investigated for the bulk states of Weyl and Dirac semimetals. The low-frequency optical conductivity of Weyl and Dirac semimetals was proposed to be linear theoretically [44,45] and verified experimentally [46–48] in the bulk systems. In addition, the optical conductivity of multi-Weyl semimetals [50] and the magneto-optical conductivity of double-Weyl semimetals [51] have also been studied, respectively. On the other hand, the finite-size effects on the optical conductivity were shown to be significant in graphene [52–55] and α-T_3 model [56]. For Dirac semimetals, it was demonstrated that Fermi arc states in a slab can mediate a large optical response [57]. However, the optical conductivity of Weyl and Dirac semimetal nanowires has not been investigated to the best of our knowledge. It is natural to wonder about what effects the Fermi arc states of nanowires would have on the optical conductivity.

In this paper, we present a theoretical study of the low-energy optical conductivity in Weyl and Dirac semimetal
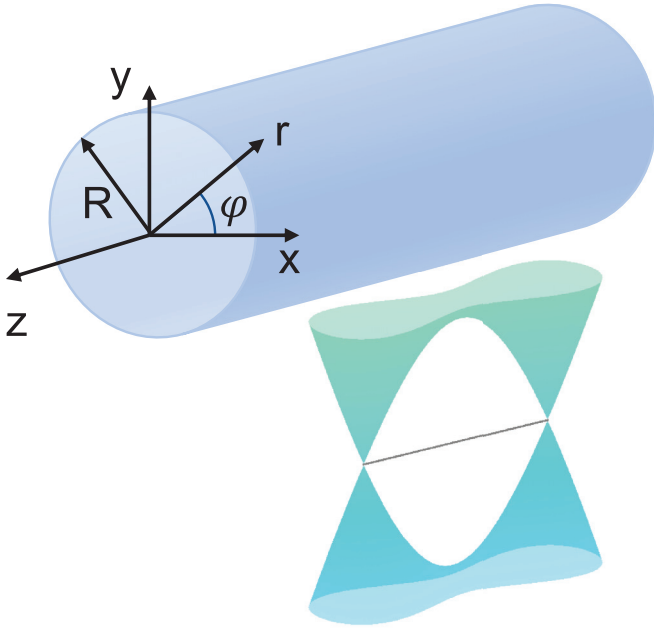
_____
*duanwy@pku.edu.cn

195436-1

FIG. 1. The schematic diagram of the nanowire and the band structure of bulk states. The nanowire is parallel to the Weyl (Dirac) nodes splitting direction (z direction).

nanowires as illustrated by Fig. 1. Since Weyl and Dirac semimetal nanowires are experimentally achievable and at the same time analytically solvable, we demonstrate that the finite-size effects and the Fermi arc states make a significant impact on the low-energy optical conductivity in a comprehensive manner. The band structure, wave functions, density of states (DOS), and the optical conductivity are calculated. Agreeing well with the results of Refs. [26,27], the Fermi arc states turn to a series of nearly flat discrete surface bands which induce the divergent DOS at low energy, and bulk states open a small gap at Weyl or Dirac points due to the finite-size effect of quantum confinements. The optical responses show strongly anisotropic depending on the polarization of the incident photon. This qualitative anisotropy is due to the strikingly different selection rules governing the quantum transitions. For an optical polarization axis parallel to the nanowire [Re(σ_{zz})], the optical transitions occur between Fermi arc and bulk bands or between bulk and bulk bands with the same total angular quantum number. Moreover, for the polarization axis perpendicular to the nanowire, the optical response Re(σ_{xx}) has a giant peak which is attributed to the additional transitions between Fermi arc and Fermi arc bands with different total angular momentum. The amplitude of this peak due to Fermi arc–Fermi arc transitions is many times stronger than those of the bulk-bulk transitions and Fermi arc–bulk transitions. Strikingly, the position of this ultrastrong response is independent of the chemical potential. This is a great advantage in adjusting the chemical potential to detect the optical conductivity dominated by Fermi arc bands. In contrast, the chemical potential is restricted in a small low-energy range in order that the longitudinal conductance of Weyl and Dirac semimetal nanowires is determined by only the Fermi arc states [26,27]. Additionally, we show that both Re(σ_{zz}) and Re(σ_{xx}) are robust to disorders. We hope that our

study would help understanding the Fermi arc contributions in the optical conductivity and provide a valuable theoretical reference for nanoelectronics and ultrafast optoelectronic applications based on nanowires of Weyl and Dirac materials.

The rest of this paper is organized as follows. In Sec. II, we introduce the low-energy effective Hamiltonian and the Kubo formula to calculate the optical conductivity. The optical conductivity is presented analytically in clean limit. The numerical results and discussion on band structures, wave functions, DOS, and the optical conductivity with finite impurity scattering rates will be presented in Sec. III. Finally, discussion and conclusion are given in Sec. IV. Calculation details are presented in the Appendixes.

TABLE I. Parameters in the effective model taken from Refs. [58,61].

	Na$_3$Bi	Cd$_3$As$_2$
M_0 (eV)	−0.08686	−0.0205
M_1 (eV Å^2)	−10.6424	−18.77
A (eV Å)	2.4598	0.889

II. HAMILTONIAN AND FORMALISM

We start from the low-energy effective Hamiltonian for electron excitations in the Dirac semimetals A_3Bi (A = Na, K, Rb) [58] and Cd$_3$As$_2$ [59] derived from $k \cdot p$ theory around the Γ point. In the basis of $|S_{J=1/2}, J_z = \frac{1}{2}\rangle$, $|S_{J=3/2}, J_z = \frac{3}{2}\rangle$, $|S_{J=1/2}, J_z = -\frac{1}{2}\rangle$, $|S_{J=3/2}, J_z = -\frac{3}{2}\rangle$, this effective model has the form [27,58–61]

$$H(\boldsymbol{p}) = \begin{pmatrix} M(\boldsymbol{p}) & \frac{A}{\hbar}p_+ & 0 & 0 \\ \frac{A}{\hbar}p_- & -M(\boldsymbol{p}) & 0 & 0 \\ 0 & 0 & M(p) & -\frac{A}{\hbar}p_- \\ 0 & 0 & -\frac{A}{\hbar}p_+ & -M(\boldsymbol{p}) \end{pmatrix}, \quad (1)$$

where $\boldsymbol{p} = (p_x, p_y, p_z)$ is the momentum, $p_\pm = p_x \pm ip_y$, and $M(\boldsymbol{p}) = M_0 - \frac{M_1}{\hbar^2}p_z^2$ with the parameters M_0, $M_1 < 0$ to reproduce band inversion, which is a vital part for the nontrivial Fermi arc. The numerical values of parameters in Hamiltonian (1) can be determined by fitting the energy spectrum with that of the first-principles calculations and are summarized in Table I [58,59,61]. Here, we omit the high-order terms $O(p_x^2)$ and $O(p_y^2)$ for simplicity and the identity matrix term which do not lead to qualitatively new effects in transport properties [27].

In the infinite system, the translation symmetry keeps for x, y, and z directions, so $\boldsymbol{k} = (k_x, k_y, k_z)$ is a good quantum number. The energy dispersion can be easily obtained:

$$E(k) = \pm\sqrt{(M_0 - M_1 k_z^2)^2 + A^2(k_x^2 + k_y^2)}. \quad (2)$$

In such a case, a pair of fourfold degenerate Dirac points locates at $\boldsymbol{k}^D = (0, 0, k_z = \pm\sqrt{\frac{M_0}{M_1}})$. Due to the block-diagonal form of Eq. (1), the 4×4 matrix could be decoupled into two 2×2 matrices, i.e., $H(\boldsymbol{p}) = \begin{pmatrix} H_{2\times2}^+(\boldsymbol{p}) & 0 \\ 0 & H_{2\times2}^-(\boldsymbol{p}) \end{pmatrix}$, where $H_{2\times2}^+(\boldsymbol{p}) = \begin{pmatrix} M_0 - \frac{M_1}{\hbar^2}p_z^2 & \frac{A}{\hbar}(p_x + ip_y) \\ \frac{A}{\hbar}(p_x - ip_y) & -M_0 + \frac{M_1}{\hbar^2}p_z^2 \end{pmatrix}$ and the lower block $H_{2\times2}^-$

could be obtained by replacing $p_x \rightarrow -p_x$ in $H_{2\times2}^+$. Each diagonal block describes a minimal time-reversal symmetry-breaking Weyl semimetal with a pair of Weyl nodes and opposite chirality [27,60]. The leading-order term of off-diagonal block takes the high-order form of $O(k^3)$ constrained by the symmetry [58,59,61]. On the other hand, the off-diagonal block can be interpreted as a momentum-dependent mass term that vanishes at the Dirac points [62,63]. Here, we concentrate on the neighborhood of $\boldsymbol{k}^D$ and only consider the expansion up to $O(k^2)$, therefore, the off-diagonal blocks can be neglected [58–60,62,63]. The Hamiltonian (1) describes 3D massless Dirac fermions. Generally, the gapless Fermi arc states of Dirac semimetals are not topologically protected. Especially, the Dirac semimetals A_3Bi (A = Na, K, Rb) and Cd$_3$As$_2$ were found to possess nontrivial surface Fermi arcs numerically [28,58,59] and were also demonstrated experimentally [32,64]. Because of a discrete up-down parity symmetry of the low-energy effective Hamiltonian, the corresponding Dirac semimetal can be identified as a Z_2 Weyl semimetal which guarantees the nontrivial surface Fermi arcs [62,63].

In order to perform analytical calculation including finite-size effects and Fermi arc states, we study a cylindrical nanowire surrounded by a vacuum or any trivial insulator. As illustrated by Fig. 1, its radius is R. It is appropriate to use the cylindrical coordinates, i.e., $r(x, y) = \sqrt{x^2 + y^2}$ and $\varphi(x, y) = \arcsin \frac{y}{\sqrt{x^2+y^2}}$. The wire is along the z axis, thus, k_z is a good quantum number, and the Fermi arc is also along the wire. The upper block Hamiltonian in the coordinate representation reads as

$$H_{2\times2}^+(r, \varphi, z) = \begin{pmatrix} M_0 - \frac{M_1}{\hbar^2}p_z^2 & -ie^{i\varphi}A\left(\frac{\partial}{\partial r} + \frac{i}{r}\frac{\partial}{\partial\varphi}\right) \\ -ie^{-i\varphi}A\left(\frac{\partial}{\partial r} - \frac{i}{r}\frac{\partial}{\partial\varphi}\right) & -M_0 + \frac{M_1}{\hbar^2}p_z^2 \end{pmatrix}.$$ (3)

We obtain the band structure and eigenfunctions by solving the Schrödinger equation $H_{2\times2}^\pm \Psi^\pm = \epsilon \Psi^\pm$ numerically. Calculation details of band structure and eigenfunctions are presented in Appendix A.

Then, the DOS could be obtained by

$$g(\epsilon) = \sum_n \int \frac{dk_z}{2\pi} \delta(\epsilon - \epsilon_{n,k_z}),$$ (4)

where $n \in \mathbb{Z}$ and $j = n - \frac{1}{2}$ is the angular momentum quantum number because that the total angular momentum operator $\widehat{J} = -i\partial_\varphi I_{2\times2} - \sigma_z/2$ commutes with Hamiltonian $H_{2\times2}^+$, $I_{2\times2}$ is the identity matrix, and σ_z is the Pauli matrix.

From the Kubo formula, the optical conductivity can be obtained [65]:

$$\sigma_{aa}(\omega) = -\frac{i\hbar}{\pi R^2} \sum_{nn'} \int \frac{dk_z}{2\pi} \int \frac{dk_z'}{2\pi} \frac{\left[f_F(\epsilon_{n,k_z}) - f_F(\epsilon_{n',k_z'})\right]\langle\Psi_{n,k_z}^+|j_a|\Psi_{n',k_z'}^+\rangle\langle\Psi_{n',k_z'}^+|j_a|\Psi_{n,k_z}^+\rangle}{(\epsilon_{n,k_z} - \epsilon_{n',k_z'})(\hbar\omega + \epsilon_{n,k_z} - \epsilon_{n',k_z'} + i\Gamma)},$$ (5)

where $f_F(\epsilon_{n,k_z}) = 1/[e^{(\epsilon_{n,k_z}-\mu)/k_B T} + 1]$ is the Fermi-Dirac distribution with the chemical potential μ at the temperature T, Γ represents the impurity scattering rate (in this paper, we assume Γ is constant for simplicity), and the current operators $j_x = \frac{ie}{\hbar}[H_{2\times2}^+, x] = \frac{eA}{\hbar}\sigma_x$, $j_y = \frac{ie}{\hbar}[H_{2\times2}^+, y] = -\frac{eA}{\hbar}\sigma_y$, and $j_z = \frac{ie}{\hbar}[H_{2\times2}^+, z] = -\frac{2e}{\hbar}M_1 k_z\sigma_z$.

In the clean limit the scattering rate $\Gamma \rightarrow 0$, the dissipative components of the conductivity tensor $\text{Re}(\sigma_{zz})$ and $\text{Re}(\sigma_{xx})$ which correspond to the absorption of light can be expressed as

$$\text{Re}[\sigma_{zz}(\omega)] = \frac{(4\pi eM_1)^2}{\hbar R^2} \sum_{n(\epsilon\neq\epsilon')} \int dk_z k_z^2 \frac{\left[f_F(\epsilon_{n,k_z}) - f_F(\epsilon_{n,k_z}')\right]}{\hbar\omega} \delta(\hbar\omega + \epsilon_{n,k_z} - \epsilon_{n,k_z}')$$

$$\times \left\{A_s(n, k_z, \epsilon_{n,k_z})A_s(n, k_z, \epsilon_{n,k_z}')\int_0^R r\,dr\left[X_n^s\left(\frac{r}{r_0}\right)X_n^s\left(\frac{r}{r_0'}\right) - F_{k_z,\epsilon_{n,k_z}}F_{k_z,\epsilon_{n,k_z}'}X_{n-1}^s\left(\frac{r}{r_0}\right)X_{n-1}^s\left(\frac{r}{r_0'}\right)\right]\right\}^2$$ (6)

and

$$\text{Re}[\sigma_{xx}(\omega)] = \frac{(2\pi eA)^2}{\hbar R^2} \sum_n \int dk_z \left\{ \begin{array}{l} \frac{[f_F(\epsilon_{n,k_z})-f_F(\epsilon_{n+1,k_z}')]}{\hbar\omega}\delta(\hbar\omega + \epsilon_{n,k_z} - \epsilon_{n+1,k_z}') \\ \times\left[A_s(n, k_z, \epsilon_{n,k_z})A_s(n+1, k_z, \epsilon_{n+1,k_z}')\int_0^R r\,dr F_{k_z,\epsilon_{n+1,k_z}'}X_n^s\left(\frac{r}{r_0'}\right)X_n^s\left(\frac{r}{r_0}\right)\right]^2 \\ +\frac{[f_F(\epsilon_{n,k_z})-f_F(\epsilon_{n-1,k_z}')]}{\hbar\omega}\delta(\hbar\omega + \epsilon_{n,k_z} - \epsilon_{n-1,k_z}') \\ \times\left[A_s(n, k_z, \epsilon_{n,k_z})A_s(n-1, k_z, \epsilon_{n-1,k_z}')\int_0^R r\,dr F_{k_z,\epsilon_{n,k_z}}X_{n-1}^s\left(\frac{r}{r_0'}\right)X_{n-1}^s\left(\frac{r}{r_0}\right)\right]^2 \end{array} \right\},$$ (7)

where $s = \text{sgn}(\alpha_{\epsilon_{n,k_z}})$, $\alpha_{\epsilon_{n,k_z}} = \epsilon_{n,k_z}^2 - (M_0 - M_1 k_z^2)^2$, $F_{k_z,\epsilon_{n,k_z}} = \sqrt{|\alpha_{\epsilon_{n,k_z}}|}/(\epsilon_{n,k_z} + M_0 - M_1 k_z^2)$, $r_0 = A/\sqrt{|\alpha_{\epsilon_{n,k_z}}|}$, $A_\pm$ are the normalization constants, $X_n^{s=+}(x) = J_n(x)$, $X_n^{s=-}(x) = I_n(x)$, and $J_n(x)$ and $I_n(x)$ are the Bessel and modified Bessel functions of the first kind, respectively.

The above optical conductivities of the nanowire show strongly anisotropic depending on the polarization axis of the incident photon. The δ functions in Eqs. (6) and (7) indicate strikingly different selection rules for $\text{Re}(\sigma_{zz})$ and $\text{Re}(\sigma_{xx})$. For $\text{Re}(\sigma_{zz})$, the transitions are allowed to occur only when $\Delta n = 0$. That is, the total angular momentum is not influenced along the z axis. On the other hand, the transitions obey selection rules $\Delta n = \pm 1$ for $\text{Re}(\sigma_{xx})$. Due to the rotational symmetry, $\text{Re}(\sigma_{yy}) = \text{Re}(\sigma_{xx})$. The above expressions of optical conductivities are too complicated to calculate analytically. Thus, we will show and elucidate the numerical
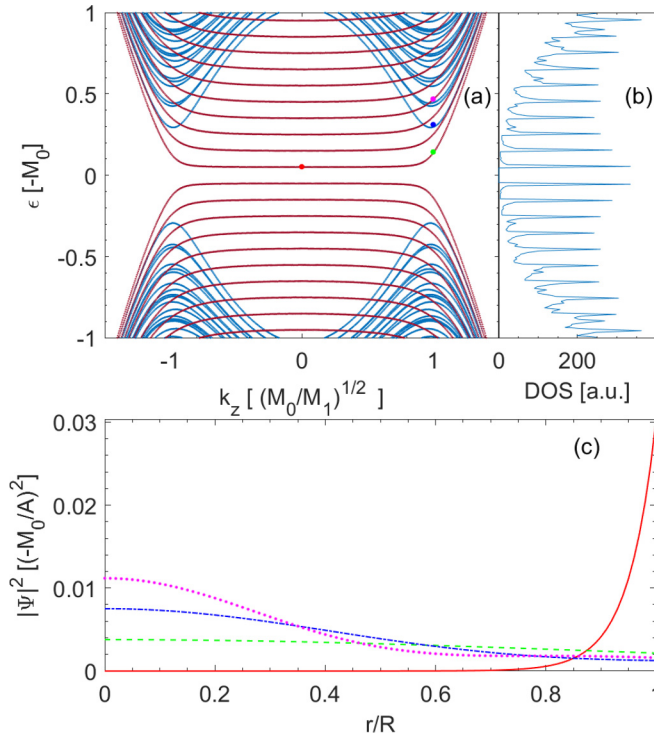
FIG. 2. (a) Band structures of $H_{2\times2}^+$ as functions of k_z with $\widetilde{R} = 10$ for $|n| \leqslant 9$. (b) The corresponding DOS of (a). (c) Wave-function profiles as functions of the radial coordinate r at $\epsilon = 0.0525$ (in units of $-M_0$), $k_z = 0$ (in units of $\sqrt{M_0/M_1}$), $\epsilon = 0.1435$, $k_z = 1$, $\epsilon = 0.3115$, $k_z = 1$, and $\epsilon = 0.4685$, $k_z = 1$, respectively. The corresponding states are labeled in (a) by the red, green, blue, and magenta dots, respectively.

results in the following section. In this work we focus on the contribution of only interband transitions to the optical conductivity. Similarly, there is a degeneracy of 2 included for Dirac semimetals including the lower block.

III. NUMERICAL RESULTS

A. Band structures and wave-function profiles

In this section, we present the numerical results. Figure 2(a) presents the band structures of $H_{2\times2}^+$ as functions of k_z with $R = \widetilde{R}A/(-M_0)$ and $\widetilde{R} = 10$. In good agreements with Ref. [27], there exhibits a series of discrete almost flat Fermi arc states with nearly equal energy space for $|k_z| < \sqrt{\frac{M_0}{M_1}}$ [see the red lines in Fig. 2(a)]. For $|k_z| > \sqrt{\frac{M_0}{M_1}}$, the Fermi arc states turn to dispersive and the energy spaces decrease gradually. The energy space of the flat Fermi arc states is $\triangle_{\text{FA}} = \frac{2A}{(2\widetilde{R}-1)A/(-M_0)} = \frac{-2M_0}{(2\widetilde{R}-1)}$ approximately. In the concrete for $\widetilde{R} = 10$, as shown in Fig. 2(a), $\triangle_{\text{FA}} \approx 0.105(-M_0)$. These nearly flat bands induce the divergent DOS as shown in Fig. 2(b). Due to the quantum confinement in nanowires, the continuum spectra of the Weyl or Dirac cones transform to a series of discrete bands as the blue lines shown in Fig. 2(a). Furthermore, there is a gap at $|E| \lesssim 0.3(-M_0)$ in which only the Fermi arc states exist because the bulk states have a

smaller confinement length $2R$ than $2\pi R$ of the Fermi arc states for a cylinder [26].

To concretely illustrate the wave-function profiles of bulk and Fermi arc states, the wave-function profile of state ϵ_{n,k_z} is given by

$$|\Psi_{n,k_z}^+|^2 = |A_+|^2 \left[\left| J_n\left(\frac{r}{r_0}\right) \right|^2 + |F(\epsilon_{n,k_z})|^2 \left| J_{n-1}\left(\frac{r}{r_0}\right) \right|^2 \right] \quad (8)$$

for $\alpha_\epsilon > 0$ and

$$|\Psi_{n,k_z}^+|^2 = |A_-|^2 \left[\left| I_n\left(\frac{r}{r_0}\right) \right|^2 + |F(\epsilon_{n,k_z})|^2 \left| I_{n-1}\left(\frac{r}{r_0}\right) \right|^2 \right] \quad (9)$$

for $\alpha_\epsilon < 0$. Figure 2(c) shows the wave-function profiles as functions of the radial coordinate r at $\epsilon = 0.0525$ (in units of $-M_0$), $k_z = 0$ (in units of $\sqrt{\frac{M_0}{M_1}}$, a Fermi arc state in the flat region, the red line), $\epsilon = 0.1435$, $k_z = 1$ (a Fermi arc state in the dispersive region, the green line), $\epsilon = 0.3115$, $k_z = 1$ (a bulk state, the blue line), and $\epsilon = 0.4685$, $k_z = 1$ (a bulk state, the magenta line), respectively. The wave function is localized to the surface for the Fermi arc state in the nearly flat region, while the wave function distributes mostly near the center of the nanowire for the bulk state.

B. Optical conductivities

The band structure of the Fermi arc and bulk states together with the optical selection rules will control the results of optical conductivities. The numerical results show that Fermi arc states play a key role in the optical conductivity. In this section, we elaborate the numerical results in a comprehensive manner.

Figures 3(b) and 3(d) show the real part of the optical conductivities σ_{zz} and σ_{xx} as functions of frequency at the neutrality condition, i.e., $\mu = 0(-M_0)$. Both $\text{Re}(\sigma_{zz})$ and $\text{Re}(\sigma_{xx})$ show series of resonant peaks. On the other hand, due to the strikingly different optical selection rules, it is found that the locations of resonant peaks in $\text{Re}(\sigma_{zz})$ and $\text{Re}(\sigma_{xx})$ are different. In order to elaborate the difference of the resonant patterns between $\text{Re}(\sigma_{zz})$ and $\text{Re}(\sigma_{xx})$, the band structures and transitions allowed by the optical selection rules are plotted in Figs. 3(a) and 3(c), respectively.

For $\text{Re}(\sigma_{zz})$, the optical selection rule is $\Delta n = 0$ because of the δ function in Eq. (6). Thus, we consider the band structure of $n = 0$ [see in Fig. 3(a)] and the corresponding optical response [see in Fig. 3(b)]. We find that there are two different types of transitions for $\text{Re}(\sigma_{zz})$. One is between Fermi arc bands and bulk bands (FA-B transitions) as marked by vertical arrows with dashed lines and plain arrowheads in Figs. 3(a) and 3(b). The corresponding optical conductivity is plotted by the dashed orange line in Fig. 3(b). Another type of the optical transitions is between bulk and bulk bands (B-B transitions) as marked by vertical arrows with dotted lines and vback arrowheads in Figs. 3(a) and 3(b). The corresponding optical conductivity is plotted by the dotted yellow line in Fig. 3(b). The total response $\text{Re}(\sigma_{zz})$ including contributions of both FA-B transitions and B-B transitions is plotted by the solid blue line in Fig. 3(b). Because of the quantum confinement effect in finite-size nanowires, the spectrum transforms to
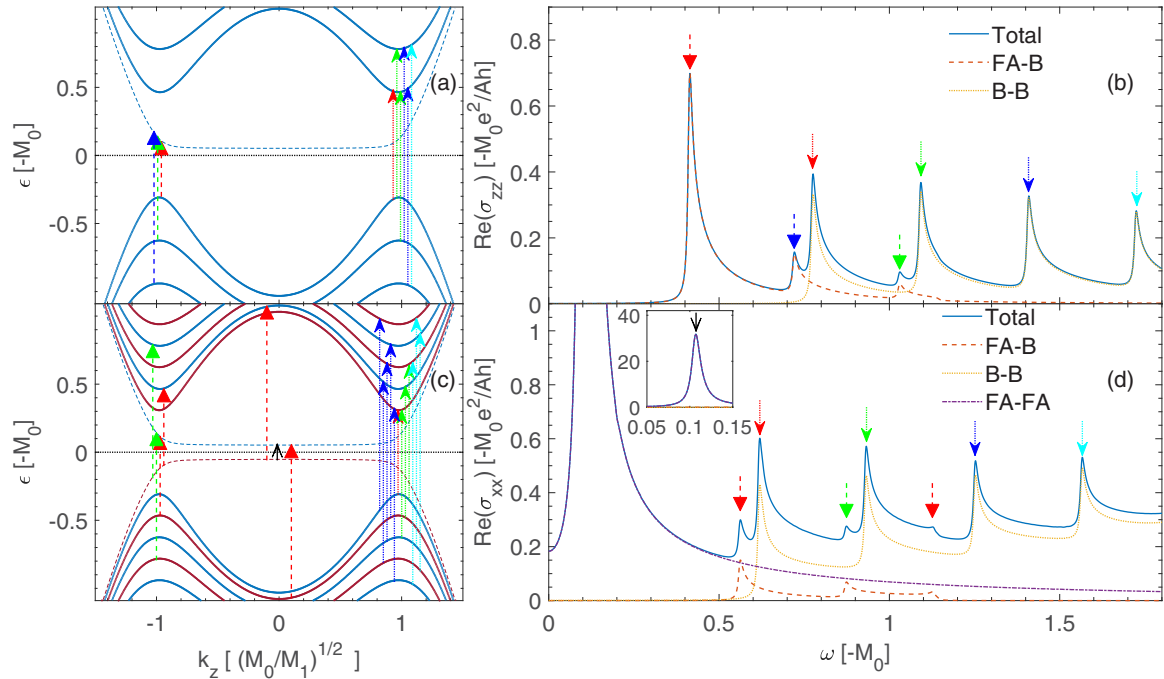
FIG. 3. (a) Band structures of $H_{2\times2}^+$ as functions of k_z with $\widetilde{R} = 10$ for $n = 0$. (b) $\mathrm{Re}(\sigma_{zz})$ as a function of frequency, corresponding to (a). (c) Band structures of $H_{2\times2}^+$ as functions of k_z with $\widetilde{R} = 10$ for $n = 0$ (blue lines) and 1 (red lines). (d) $\mathrm{Re}(\sigma_{xx})$ as a function of frequency, corresponding to (c). The allowed transitions between bands are shown schematically for $\mathrm{Re}(\sigma_{zz})$ and $\mathrm{Re}(\sigma_{xx})$ in (a) and (c), respectively. In (a) and (c), the FA-B, B-B, and FA-FA transitions are indicated by vertical arrows of dashed lines with plain arrowheads, dotted lines with vback arrowheads, and solid line with thin vback arrowhead, respectively. The corresponding peaks in optical conductivities are marked by vertical arrows with the same color, line styles, and arrowhead styles in (b) and (d), respectively. The inset of Fig. 3(d) shows an enlarged view of $\mathrm{Re}(\sigma_{xx})$ near the FA-FA transition. The other parameters are $\mu = 0(-M_0)$, $T = 10$ K, and $\Gamma = 0.005(-M_0)$.

discrete dispersive bands with extrema and there shows a gap between the Fermi arc band and the valence bulk bands. The first and highest response peak of $\mathrm{Re}(\sigma_{zz})$ is attributed to the FA-B transitions and locates at the frequency corresponding to the gap as shown by the vertical arrows with red dashed lines and plain arrowheads in Figs. 3(a) and 3(b). The amplitude of the response peaks due to FA-B transitions decreases faster than that of B-B transitions. These asymmetry resonant peaks begin with vertical jumps because of the extrema of discrete bands and then decrease with increasing ω due to the dispersive band structure. The tails of these resonant peaks overlap with the new peaks at higher frequencies.

On the other hand, the optical selection rule is $\Delta n = \pm 1$ for $\mathrm{Re}(\sigma_{xx})$, which is strikingly different from $\mathrm{Re}(\sigma_{zz})$. The transitions can only occur between different angular momentum with $\Delta n = \pm 1$. Therefore, the $n = 0$ (blue lines) and 1 (red lines) bands are plotted in Fig. 3(c). Correspondingly, patterns of optical resonant peaks in $\mathrm{Re}(\sigma_{xx})$ [see Fig. 3(d)] express completely different characteristics from $\mathrm{Re}(\sigma_{zz})$. These manifest a strong anisotropy of the optical conductivities. Similar with $\mathrm{Re}(\sigma_{zz})$, FA-B transitions, B-B transitions, and the corresponding resonant peaks are indicated by vertical arrows in Figs. 3(c) and 3(d), respectively. Figure 3(d) shows that the amplitude of resonant peaks due to FA-B transitions is weaker than those due to B-B transitions. Additionally, $\mathrm{Re}(\sigma_{xx})$ shows a giant optical resonant peak due to the transitions between Fermi arc and Fermi arc states (FA-FA transitions) as marked by the black arrow in the inset of Fig. 3(d). The inset of Fig. 3(d) is an enlarged view of

$\mathrm{Re}(\sigma_{xx})$ near the FA-FA transitions. Due to the divergence of the DOS of the near-flat Fermi arc bands, a large set of FA-FA transitions occurs. As a result, the amplitude of this resonant peak is many times stronger than other resonant peaks induced by FA-B and B-B transitions. This is a prominent feature of $\mathrm{Re}(\sigma_{xx})$ and one of the key results of this paper. Furthermore, this ultrastrong response is situated at the frequency $\omega = 0.105(-M_0)$ which is exact the confinement gap of Fermi arc states [see the black arrow in Fig. 3(c)]. This confinement gap stems from the finite-size effect of nanowires. Interestingly, this ultrastrong peak position is independent of the chemical potential as shown in Fig. 4 and this peculiar characteristic will be elucidated in the following.

In Fig. 4, we plot the optical conductivities $\mathrm{Re}(\sigma_{zz})$ and $\mathrm{Re}(\sigma_{xx})$ as functions of frequency for four values of the chemical potential. Figure 5 further illustrates the effect of the chemical potential μ on the optical conductivities $\mathrm{Re}(\sigma_{zz})$ and $\mathrm{Re}(\sigma_{xx})$ by plotting the contributions of the FA-B, B-B, and FA-FA transitions, respectively. Several salient features of the optical conductivities for nonzero values of chemical potential are worth being discussed.

For $\mathrm{Re}(\sigma_{zz})$, as μ is tuned to $0.13(-M_0)$, the lowest peak due to FA-B transitions [see Figs. 5(a1) and 5(a2)] is suppressed and the rest of the curve is unaffected. Parts of interband transitions B $\rightarrow$ FA of $n = 0$ are forbidden by Pauli blocking. On the other hand, parts of the intraband transitions FA $\rightarrow$ B of $n = 0$ are now allowed because the nearly flat parts of $n = 0$ Fermi arc band get occupied while the conduction parts of the bulk bands remain empty. As a result,
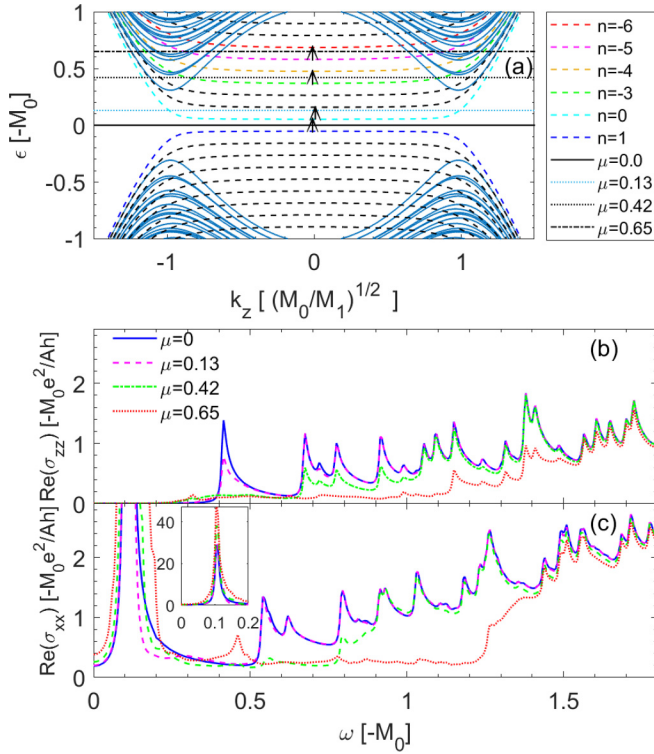
FIG. 4. (a) Band structures of $H_{2\times 2}^+$ as functions of k_z with $\widetilde{R} =$ 10 for $|n| \leqslant 9$. The chemical potentials $\mu = 0, 0.13, 0.42, 0.65$ (in units of $-M_0$) are labeled as black solid, light blue dotted, black dotted, and black dotted-dashed lines, respectively. The corresponding allowed FA-FA transitions are shown schematically for $\mathrm{Re}(\sigma_{xx})$. The real part of optical conductivities (b) σ_{zz} and (c) σ_{xx} as functions of frequency for chemical potentials $\mu = 0, 0.13, 0.42, 0.65$ (in units of $-M_0$). The other parameters are $T = 10$ K and $\Gamma = 0.005(-M_0)$.

FIG. 5. The plot of (a1)–(a4) $\mathrm{Re}(\sigma_{zz})$ (considering total, FA-B, and B-B transitions separately) and (b1)–(b4) $\mathrm{Re}(\sigma_{xx})$ (considering total, FA-B, B-B, and FA-FA transitions separately) as functions of frequency for several values of the chemical potential $\mu = 0, 0.13, 0.42, 0.65$ (in units of $-M_0$), respectively. The other parameters are $T = 10$ K and $\Gamma = 0.005(-M_0)$.

the absorption edge will appear at lower frequency as shown in Fig. 5(a2). Similarly, for $\mathrm{Re}(\sigma_{xx})$ and increasing μ further, the optical conductivities at low frequencies are modified due to the intraband transitions allowed and parts of interband transitions forbidden as shown in Figs. 4 and 5. The results at high frequency are unaffected.

Moreover, there presents a significant feature for $\mathrm{Re}(\sigma_{xx})$ that no matter μ locates in the bulk gap or not, the ultrastrong resonant peak due to FA-FA transitions persists and its location is not influenced. This is because the Fermi arc states are equispaced $\triangle_{\mathrm{FA}} = \frac{-2M_0}{(2R-1)} \approx 0.105(-M_0)$ and the selection rule for $\mathrm{Re}(\sigma_{xx})$ is $\Delta n = \pm 1$. The allowed FA-FA transitions are indicated by the black arrows in Fig. 4(a). Additionally, the height of this ultrastrong peak at $\omega \approx 0.105(-M_0)$ is enhanced by increasing μ due to three reasons. First, Fermi arc bands are nearly flat near $|k_z| = 0$. With $|k_z|$ increasing, the $n \leqslant 0$ Fermi arc bands curve up while the $n > 0$ Fermi arc bands curve down. For $\mu = 0$, the $n = 0$ Fermi arc band curves up and the $n = 1$ curves down. For $\mu = 0.13(-M_0)$, both the $n = 0$ and -1 bands curve up. Therefore, the region of nearly parallel Fermi arc bands with the space $\triangle_{\mathrm{FA}}$ for $\mu = 0.13(-M_0)$ is larger than for $\mu = 0.0$. Second, for $\mu = 0$, only the transitions between $n = 0 \rightarrow -1$ contribute to the ultrastrong peak. In contrast, for $\mu = 0.65(-M_0)$, aside from the major contribution of transitions $n = -5 \rightarrow -6$, there also
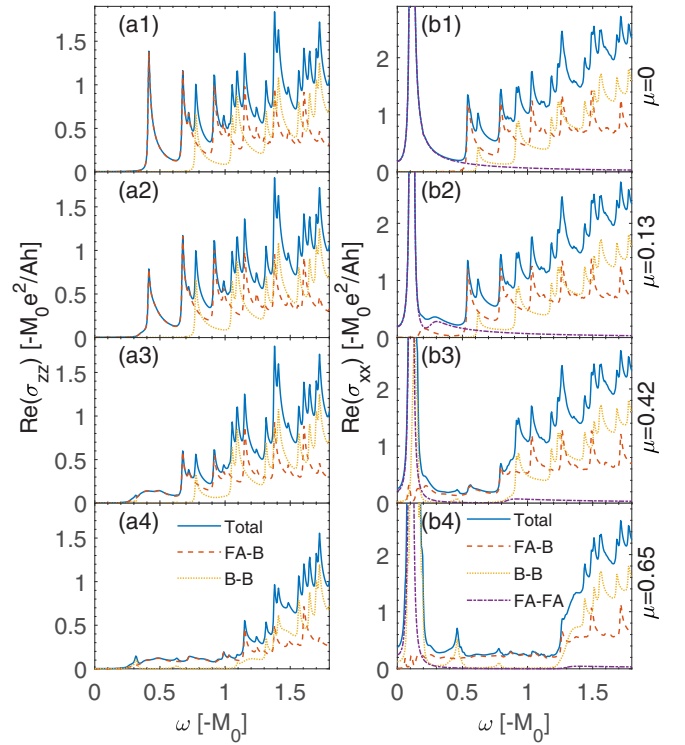
include transitions $n = -4 \rightarrow -5, -3 \rightarrow -4, \dots$ and until $n = 0 \rightarrow -1$, which are allowed because of the dispersive Fermi arc bands. Finally, the additional contributions of the B-B transitions enhance the peak as shown in Figs. 5(b3) and 5(b4). As was emphasized in Refs. [26,27], the finite-size effect of nanowires makes it possible to probe DC which is dominated by the Fermi arc state. However, the chemical potential should be tuned low enough in the bulk gap. Here, we find that the ultrastrong peak of optical conductivity $\mathrm{Re}(\sigma_{xx})$ due to FA-FA transitions is independent of chemical potentials. This distinctive qualitative feature provides an optical means to probe the dynamics of the Fermi arc states in Weyl and Dirac nanowires. And there shows an advantage in tuning the chemical potential.

At last, we examine the effect of disorders on the features above by increasing the scattering rate Γ. Figure 6 shows that increasing the scattering rate Γ, both $\mathrm{Re}(\sigma_{zz})$ and $\mathrm{Re}(\sigma_{xx})$ remain qualitatively unaffected except that the resonant peaks are suppressed and blurred out to smoother. The peak height and peak width of the ultrastrong peaks of $\mathrm{Re}(\sigma_{xx})$ in Fig. 6 as functions of scattering rate Γ are shown in Fig. 7(a). The peak width is defined at half-height. On the other hand, Fig. 7(b) shows the ratio of the peak height of the ultrastrong peak (H_0) to that of the neighboring rsonance (H_1) of $\mathrm{Re}(\sigma_{xx})$ in Fig. 6 as functions of scattering rate Γ. By increasing the scattering rate, both the peak height and the ratio decrease rapidly. Even for $\Gamma = 0.08(-M_0)$, H_0 is still stronger than
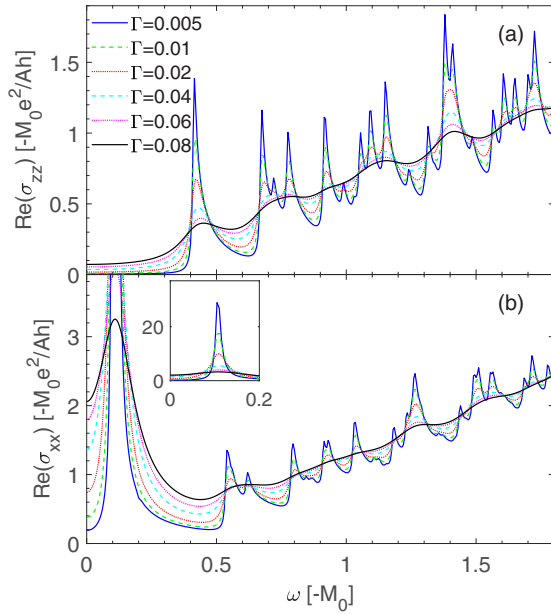
FIG. 6. The plot of (a) $\mathrm{Re}(\sigma_{zz})$ and (b) $\mathrm{Re}(\sigma_{xx})$ as functions of frequency for several values of scattering rate Γ (in units of $-M_0$). The other parameters are $T = 10$ K and $\mu = 0(-M_0)$.

H_1. For Na$_3$Bi, $M_0 = -0.086\,86$ eV [58], this corresponds to a scattering rate of $\Gamma \approx 6.95$ meV. At the same time, the peak width increases nearly linearly as the orange dashed line shown in Fig. 7(a) which is the linear fit for the peak width. In a word, the characteristic ultrastrong peak due to FA-FA transitions of $\mathrm{Re}(\sigma_{xx})$ and the anisotropic behaviors of the optical conductivities are stable with disorders.

IV. DISCUSSION AND CONCLUSION

Now we give a brief estimation of the relevant optical frequency. For specified materials, the frequency at which the characteristic giant peak is located is dependent on the
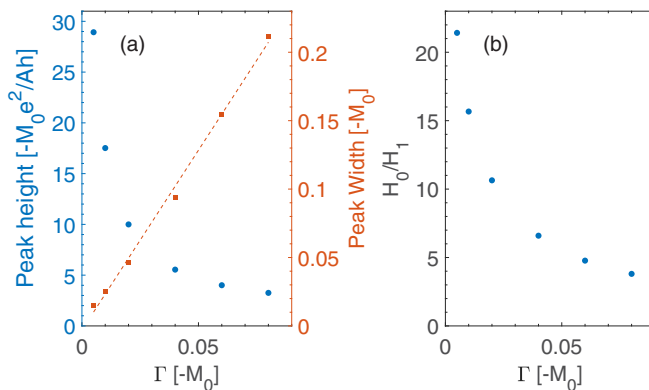

FIG. 7. The plot of (a) peak height (light blue circle) and peak width (orange square) of the ultrastrong peak of $\mathrm{Re}(\sigma_{xx})$ in Fig. 6, (b) the ratio of the peak height between the ultrastrong peak and the nearest peak of $\mathrm{Re}(\sigma_{xx})$ in Fig. 6 as functions of scattering rate Γ. The orange dashed line in (a) is the linear fit for the peak width. The other parameters are the same with Fig. 6.

radius of the nanowire and material parameters. The parameters used for Na$_3$Bi and Cd$_3$As$_2$ in the following estimation are summarized in Table I. For Na$_3$Bi, $M_0 = -0.086\,86$ eV and $A = 2.4598$ eV Å [58]. The radius is $R = 10A/(-M_0) \approx 28.219$ nm. The characteristic giant peak is estimated to be located at $\omega \approx 0.105(-M_0) \approx 9.12$ meV corresponding to 2.22×10^{12} Hz. For Cd$_3$As$_2$, $M_0 = -0.0205$ eV and $A = 0.889$ eV Å [61]. The radius is $R \approx 43.366$ nm approximately and the characteristic giant peak is located at $\omega \approx 2.15$ meV corresponding to 0.525×10^{12} Hz. The radii for both materials are accessible in experiments [15,16,19,66]. The adequate light of the optical experiment for both materials falls into the terahertz regime.

In summary, we have performed a systematic study on the optical conductivity of Weyl and Dirac semimetal nanowires theoretically and demonstrated that the Fermi arc states play a key role in the optical conductivity. Due to the finite-size effect of nanowires, the continuum spectra of the Weyl or Dirac cones transform into a series of discrete bands. There exhibits a series of discrete and equispaced almost flat Fermi arc states which attribute to the divergence of the DOS. Because the bulk states have a smaller confinement length $2R$ than $2\pi R$ of the Fermi arc states for a cylinder nanowire [26], there is a gap of the bulk bands in which only the Fermi arc states exist. These results of band structures are in good agreements with Refs. [26,27].

These particular band structures of nanowires, together with the strikingly different selection rules of $\mathrm{Re}(\sigma_{zz})$ and $\mathrm{Re}(\sigma_{xx})$, result in the strong anisotropy of optical conductivities. Therefore, $\mathrm{Re}(\sigma_{zz})$ and $\mathrm{Re}(\sigma_{xx})$ show different patterns of resonant peaks. For $\mathrm{Re}(\sigma_{zz})$, the optical selection rule is $\triangle n = 0$, thus only FA-B and B-B transitions are allowed. However, the situation is quite different for $\mathrm{Re}(\sigma_{xx})$. For $\mathrm{Re}(\sigma_{xx})$, the optical selection rule is $\triangle n = \pm 1$. Aside from FA-B and B-B transitions, there are additional FA-FA transitions for $\mathrm{Re}(\sigma_{xx})$. Because of the nearly flat and equispaced Fermi arc states, a large set of FA-FA transitions occurs and induces a giant resonant peak. The amplitude of this giant resonant peak is many times stronger than that of other transitions. The position of this giant resonant peak is at the frequency $\omega = 0.105(-M_0)$ which is exact the confinement gap of Fermi arc states $\triangle_{\mathrm{FA}} = \frac{-2M_0}{(2\widetilde{R}-1)} \approx 0.105(-M_0)$ for $\widetilde{R} = 10$. Therefore, the peak position is independent of the chemical potential. This ultrastrong low-frequency resonant peak of $\mathrm{Re}(\sigma_{xx})$ provides an optical means to probe the dynamics of the Fermi arc states in Weyl and Dirac nanowires. A large contribution of the Fermi arc states to the longitudinal conductance of Weyl semimetal nanowires was reported by Refs. [26,27] in which the chemical potentials were restricted in a small low-energy range, i.e., in the bulk gap. Our results exhibit a great advantage in adjusting the chemical potential. At last, we show that the characteristic features of both $\mathrm{Re}(\sigma_{zz})$ and $\mathrm{Re}(\sigma_{xx})$ are robust to disorders.

Additionally, we analyze the effect of the magnetic field along the wire axis on the Fermi arc stated briefly in Appendix B. The magnetic flux enters effectively through the shift $n \rightarrow n + \Phi$ [24]. This shift induces the shift of the nearly flat bands of Fermi arc states, while the space between the Fermi arc states is unchanged. Therefore, the position of the characteristic ultrastrong resonant peak of $\mathrm{Re}(\sigma_{xx})$ which

is determined by the space between Fermi arc states $\triangle_{\mathrm{FA}}$ is unaffected.

We propose the optical absorption experiment as a presently available method to detect the signature of Fermi arc states in Weyl or Dirac nanowires. Moreover, we hope that our findings could provide a valuable theoretical reference for nanoelectronics and ultrafast optoelectronic applications based on nanowires of Weyl and Dirac materials.

APPENDIX A: BAND STRUCTURE AND EIGENFUNCTIONS

Solving the Schrödinger equation $H_{2\times2}^+\Psi^+ = \epsilon\Psi^+$, the eigenfunctions are found in the form

$$\Psi_{n,k_z}^+(r,\varphi,z) = \begin{pmatrix} \rho_-(r)e^{i(n)\varphi} \\ \rho_+(r)e^{i(n-1)\varphi} \end{pmatrix}\frac{e^{ik_zz}}{\sqrt{L_z}}, \quad (A1)$$

where $j = n - \frac{1}{2}$ is the angular momentum quantum number because the total angular momentum operator $\widehat{J} = -i\partial_\varphi I_{2\times2} - \sigma_z/2$ commutes with Hamiltonian $H_{2\times2}^+$, $I_{2\times2}$ is the identity matrix, σ_z is the Pauli matrix, and $n \in \mathbb{Z}$. In the case of $\alpha_\epsilon > 0$, $\rho_\mp(r)$ are

$$\rho_-(r) = A_+ J_n\left(\frac{\sqrt{|\alpha_\epsilon|}}{A}r\right), \quad (A2)$$

$$\rho_+(r) = -iA_+\frac{\sqrt{|\alpha_\epsilon|}}{\epsilon + M_0 - M_1 k_z^2}J_{n-1}\left(\frac{\sqrt{|\alpha_\epsilon|}}{A}r\right), \quad (A3)$$

and in the case of $\alpha_\epsilon < 0$, $\rho_\mp(r)$ are

$$\rho_-(r) = A_- I_n\left(\frac{\sqrt{|\alpha_\epsilon|}}{A}r\right), \quad (A4)$$

$$\rho_+(r) = -iA_-\frac{\sqrt{|\alpha_\epsilon|}}{\epsilon + M_0 - M_1 k_z^2}I_{n-1}\left(\frac{\sqrt{|\alpha_\epsilon|}}{A}r\right), \quad (A5)$$

where $\alpha_\epsilon = \epsilon^2 - (M_0 - M_1 k_z^2)^2$, $A_\pm$ are the normalization constants, $J_n(x)$ and $I_n(x)$ are the Bessel and modified Bessel functions of the first kind, respectively.

As illustrated by Fig. 1, we study a cylindrical nanowire surrounded by a vacuum or any trivial insulator and its radius is R defined by $r = \sqrt{x^2 + y^2} \leqslant R$. Following Refs. [26,27,67], the outside of the nanowire with $r > R$

is modeled by replacing $M_0 \to \tilde{M}_0$ and setting $\tilde{M}_0 \to \infty$. Matching the wave functions at the surface $r = R$, the boundary condition is obtained in the form

$$[\rho_-(r) + i\rho_+(r)]|_{r=R} = 0. \quad (A6)$$

Note that a general form of the boundary condition in cylindrical nanowires was shown in Refs. [24,68,69]. The shape of the Fermi arc states is sensitive to boundary conditions [24]. While the boundary condition (A6) here is a special case of the general form, the Fermi arc states have a good agreement with the result of the lattice model with zero boundary conditions (also known as open or hard-wall boundary conditions) [7,8,26].

Substituting the wave functions (A2)–(A5) into the above boundary condition (A6), we obtain

$$J_n\left(\frac{\sqrt{|\alpha_\epsilon|}}{A}R\right) + \frac{\sqrt{|\alpha_\epsilon|}}{\epsilon + M_0 - M_1 k_z^2}J_{n-1}\left(\frac{\sqrt{|\alpha_\epsilon|}}{A}R\right) = 0 \quad (A7)$$

for $\alpha_\epsilon > 0$ and

$$I_n\left(\frac{\sqrt{|\alpha_\epsilon|}}{A}R\right) + \frac{\sqrt{|\alpha_\epsilon|}}{\epsilon + M_0 - M_1 k_z^2}I_{n-1}\left(\frac{\sqrt{|\alpha_\epsilon|}}{A}R\right) = 0 \quad (A8)$$

for $\alpha_\epsilon < 0$. The details of this analytical approach were described thoroughly in Ref. [27]. For given n and k_z, the above Eqs. (A7) and (A8) could be solved numerically and yield the allowed energies which are the band structures of a Weyl nanowire. Similarly, for the lower block there are $H_{2\times2}^-(r,\varphi,z) = [H_{2\times2}^+(r,\varphi,z)]^*$ and $\Psi_{n,k_z}^-(r,\varphi,z) = [\Psi_{n,k_z}^+(r,\varphi,z)]^*$.

APPENDIX B: THE EFFECT OF A CONSTANT MAGNETIC FIELD ALONG THE NANOWIRE AXIS

In this Appendix, we analyze the effect of a constant magnetic field along the nanowire axis. The magnetic flux is included by replacing $\boldsymbol{p}$ with $\boldsymbol{\pi} = \boldsymbol{p} + e\boldsymbol{A}$, where $\boldsymbol{A} = \frac{B}{2}(-y, x, 0)$. In the cylindrical coordinates, we obtain

$$\pi_x \pm i\pi_y = -ie^{\pm i\varphi}A\left[\frac{\partial}{\partial r} \mp \frac{1}{r}\left(-i\frac{\partial}{\partial\varphi} + \frac{eBr^2}{2\hbar}\right)\right]. \quad (B1)$$

Because the Fermi arc states mostly locate at the surface, we take the approximation $r \to R$. The magnetic flux through the nanowire is $\Phi = \frac{eBR^2}{2\hbar} = \frac{\pi R^2 B}{\phi_0}$, where $\phi_0 = h/e$ is the magnetic flux quantum. Thus, we obtain

$$\pi_x \pm i\pi_y = -ie^{\pm i\varphi}A\left[\frac{\partial}{\partial r} \mp \frac{1}{R}\left(-i\frac{\partial}{\partial\varphi} + \Phi\right)\right] \quad (B2)$$

and the Hamiltonian (3) in the cylindrical coordinates is

$$H_{2\times2}^+(r,\varphi,z) = \begin{pmatrix} M_0 - \frac{M_1}{\hbar^2}p_z^2 & -ie^{i\varphi}A\left[\frac{\partial}{\partial r} - \frac{1}{R}\left(-i\frac{\partial}{\partial\varphi} + \Phi\right)\right] \\ -ie^{-i\varphi}A\left[\frac{\partial}{\partial r} + \frac{1}{R}\left(-i\frac{\partial}{\partial\varphi} + \Phi\right)\right] & -M_0 + \frac{M_1}{\hbar^2}p_z^2 \end{pmatrix}. \quad (B3)$$

Considering that the eigenfunctions are in the form

$$\Psi_{n,k_z}^+(r,\varphi,z) = \begin{pmatrix} \rho_-(r)e^{i(n)\varphi} \\ \rho_+(r)e^{i(n-1)\varphi} \end{pmatrix}\frac{e^{ik_zz}}{\sqrt{L_z}}, \quad (B4)$$

the magnetic flux enters the band structure of Fermi arc states through the shift $n \to n + \Phi$ effectively [24].

[1] N. P. Armitage, E. J. Mele, and A. Vishwanath, Weyl and Dirac semimetals in three-dimensional solids, Rev. Mod. Phys. **90**, 015001 (2018).

[2] B. Q. Lv, T. Qian, and H. Ding, Experimental perspective on three-dimensional topological semimetals, Rev. Mod. Phys. **93**, 025002 (2021).

[3] M. Z. Hasan, S.-Y. Xu, I. Belopolski, and S.-M. Huang, Discovery of Weyl fermion semimetals and topological Fermi arc states, Annu. Rev. Condens. Matter Phys. **8**, 289 (2017).

[4] H. Zheng and M. Zahid Hasan, Quasiparticle interference on type-I and type-II Weyl semimetal surfaces: A review, Adv. Phys. X **3**, 1466661 (2018).

[5] S. A. Parameswaran, T. Grover, D. A. Abanin, D. A. Pesin, and A. Vishwanath, Probing the chiral anomaly with nonlocal transport in three-dimensional topological semimetals, Phys. Rev. X **4**, 031035 (2014).

[6] Y. Baum, E. Berg, S. A. Parameswaran, and A. Stern, Current at a distance and resonant transparency in Weyl semimetals, Phys. Rev. X **5**, 041046 (2015).

[7] Y. Ominato and M. Koshino, Magnetotransport in Weyl semimetals in the quantum limit: Role of topological surface states, Phys. Rev. B **93**, 245304 (2016).

[8] A. Igarashi and M. Koshino, Magnetotransport in Weyl semimetal nanowires, Phys. Rev. B **95**, 195306 (2017).

[9] J. Behrends, S. Roy, M. H. Kolodrubetz, J. H. Bardarson, and A. G. Grushin, Landau levels, Bardeen polynomials, and Fermi arcs in Weyl semimetals: Lattice-based approach to the chiral anomaly, Phys. Rev. B **99**, 140201(R) (2019).

[10] P. Baireuther, J. Tworzydło, M. Breitkreiz, İ. Adagideli, and C. Beenakker, Weyl-Majorana solenoid, New J. Phys. **19**, 025006 (2017).

[11] P. Baireuther, J. A. Hutasoit, J. Tworzydło, and C. W. J. Beenakker, Scattering theory of the chiral magnetic effect in a Weyl semimetal: interplay of bulk Weyl cones and surface Fermi arcs, New J. Phys. **18**, 045009 (2016).

[12] E. V. Gorbar, V. A. Miransky, I. A. Shovkovy, and P. O. Sukhachov, Origin of dissipative Fermi arc transport in Weyl semimetals, Phys. Rev. B **93**, 235127 (2016).

[13] H. Inoue, A. Gyenis, Z. Wang, J. Li, S. W. Oh, S. Jiang, N. Ni, B. A. Bernevig, and A. Yazdani, Quasiparticle interference of the Fermi arcs and surface-bulk connectivity of a Weyl semimetal, Science **351**, 1184 (2016).

[14] B. Fu, H.-W. Wang, and S.-Q. Shen, Quantum interference theory of magnetoresistance in Dirac materials, Phys. Rev. Lett. **122**, 246601 (2019).

[15] L.-X. Wang, C.-Z. Li, D.-P. Yu, and Z.-M. Liao, Aharonov–Bohm oscillations in Dirac semimetal Cd₃As₂ nanowires, Nat. Commun. **7**, 10769 (2016).

[16] L.-X. Wang, S. Wang, J.-G. Li, C.-Z. Li, D. Yu, and Z.-M. Liao, Universal conductance fluctuations in Dirac semimetal Cd₃As₂ nanowires, Phys. Rev. B **94**, 161402(R) (2016).

[17] B.-C. Lin, S. Wang, L.-X. Wang, C.-Z. Li, J.-G. Li, D. Yu, and Z.-M. Liao, Gate-tuned Aharonov-Bohm interference of surface states in a quasiballistic Dirac semimetal nanowire, Phys. Rev. B **95**, 235436 (2017).

[18] L.-X. Wang, S. Wang, J.-G. Li, C.-Z. Li, J. Xu, D. Yu, and Z.-M. Liao, Magnetotransport properties near the Dirac point of Dirac semimetal Cd₃As₂ nanowires, J. Phys.: Condens. Matter **29**, 044003 (2017).

[19] S. Wang, B.-C. Lin, W.-Z. Zheng, D. Yu, and Z.-M. Liao, Fano interference between bulk and surface states of a Dirac semimetal Cd₃As₂ nanowire, Phys. Rev. Lett. **120**, 257701 (2018).

[20] B.-C. Lin, S. Wang, A.-Q. Wang, Y. Li, R.-R. Li, K. Xia, D. Yu, and Z.-M. Liao, Electric control of Fermi arc spin transport in individual topological semimetal nanowires, Phys. Rev. Lett. **124**, 116802 (2020).

[21] C.-Z. Li, A.-Q. Wang, C. Li, W.-Z. Zheng, A. Brinkman, D.-P. Yu, and Z.-M. Liao, Topological transition of superconductivity in Dirac semimetal nanowire Josephson junctions, Phys. Rev. Lett. **126**, 027001 (2021).

[22] M. Breitkreiz and P. W. Brouwer, Large contribution of fermi arcs to the conductivity of topological metals, Phys. Rev. Lett. **123**, 066804 (2019).

[23] G. Resta, S.-T. Pi, X. Wan, and S. Y. Savrasov, High surface conductivity of Fermi-arc electrons in Weyl semimetals, Phys. Rev. B **97**, 085142 (2018).

[24] A. De Martino, K. Dorn, F. Buccheri, and R. Egger, Phonon-induced magnetoresistivity of Weyl semimetal nanowires, Phys. Rev. B **104**, 155425 (2021).

[25] N. L. Nair, M.-E. Boulanger, F. Laliberté, S. Griffin, S. Channa, A. Legros, W. Tabis, C. Proust, J. Neaton, L. Taillefer, and J. G. Analytis, Signatures of possible surface states in TaAs, Phys. Rev. B **102**, 075402 (2020).

[26] V. Kaladzhyan and J. H. Bardarson, Quantized Fermi arc mediated transport in Weyl semimetal nanowires, Phys. Rev. B **100**, 085424 (2019).

[27] P. O. Sukhachov, M. V. Rakov, O. M. Teslyk, and E. V. Gorbar, Fermi arcs and DC transport in nanowires of dirac and weyl semimetals, Ann. Phys. (Berlin) **532**, 1900449 (2020).

[28] A. C. Potter, I. Kimchi, and A. Vishwanath, Quantum oscillations from surface Fermi arcs in Weyl and Dirac semimetals, Nat. Commun. **5**, 5161 (2014).

[29] E. V. Gorbar, V. A. Miransky, I. A. Shovkovy, and P. O. Sukhachov, Quantum oscillations as a probe of interaction effects in Weyl semimetals in a magnetic field, Phys. Rev. B **90**, 115131 (2014).

[30] D. Bulmash and X.-L. Qi, Quantum oscillations in Weyl and Dirac semimetal ultrathin films, Phys. Rev. B **93**, 081103 (2016).

[31] M.-X. Deng, G. Y. Qi, R. Ma, R. Shen, R.-Q. Wang, L. Sheng, and D. Y. Xing, Quantum oscillations of the positive longitudinal magnetoconductivity: A fingerprint for identifying Weyl semimetals, Phys. Rev. Lett. **122**, 036601 (2019).

[32] P. J. Moll, N. L. Nair, T. Helm, A. C. Potter, I. Kimchi, A. Vishwanath, and J. G. Analytis, Transport evidence for Fermi-arc-mediated chirality transfer in the Dirac semimetal Cd₃As₂, Nature (London) **535**, 266 (2016).

[33] Y. Zhang, D. Bulmash, P. Hosur, A. C. Potter, and A. Vishwanath, Quantum oscillations from generic surface Fermi arcs and bulk chiral modes in Weyl semimetals, Sci. Rep. **6**, 23741 (2016).

[34] R. Chen, T. Liu, C. M. Wang, H.-Z. Lu, and X. C. Xie, Field-tunable one-sided higher-order topological hinge states in Dirac semimetals, Phys. Rev. Lett. **127**, 066801 (2021).

[35] C. M. Wang, H.-P. Sun, H.-Z. Lu, and X. C. Xie, 3D quantum hall effect of fermi arcs in topological semimetals, Phys. Rev. Lett. **119**, 136806 (2017).

[36] M. Uchida, Y. Nakazawa, S. Nishihaya, K. Akiba, M. Kriener, Y. Kozuka, A. Miyake, Y. Taguchi, M. Tokunaga, N. Nagaosa *et al.*, Quantum Hall states observed in thin films of Dirac semimetal Cd_3As_2, Nat. Commun. **8**, 2274 (2017).

[37] C. Zhang, A. Narayan, S. Lu, J. Zhang, H. Zhang, Z. Ni, X. Yuan, Y. Liu, J.-H. Park, E. Zhang *et al.*, Evolution of Weyl orbit and quantum Hall effect in Dirac semimetal Cd_3As_2, Nat. Commun. **8**, 1272 (2017).

[38] S. Nishihaya, M. Uchida, Y. Nakazawa, R. Kurihara, K. Akiba, M. Kriener, A. Miyake, Y. Taguchi, M. Tokunaga, and M. Kawasaki, Quantized surface transport in topological Dirac semimetal films, Nat. Commun. **10**, 2564 (2019).

[39] C. Zhang, Y. Zhang, X. Yuan, S. Lu, J. Zhang, A. Narayan, Y. Liu, H. Zhang, Z. Ni, R. Liu *et al.*, Quantum Hall effect based on Weyl orbits in Cd_3As_2, Nature (London) **565**, 331 (2019).

[40] T. Schumann, L. Galletti, D. A. Kealhofer, H. Kim, M. Goyal, and S. Stemmer, Observation of the quantum hall effect in confined films of the three-dimensional Dirac semimetal Cd_3As_2, Phys. Rev. Lett. **120**, 016801 (2018).

[41] H. Li, H. Liu, H. Jiang, and X. C. Xie, 3D quantum hall effect and a global picture of edge states in Weyl semimetals, Phys. Rev. Lett. **125**, 036602 (2020).

[42] F. Buccheri, A. De Martino, R. G. Pereira, P. W. Brouwer, and R. Egger, Phonon-limited transport and Fermi arc lifetime in Weyl semimetals, Phys. Rev. B **105**, 085410 (2022).

[43] I. Cohn, S. G. Zybtsev, A. P. Orlov, and S. V. Zaitsev-Zotov, Magnetoresistance in Quasi-One-Dimensional Weyl Semimetal $(TaSe_4)_2I$, JETP Lett. **112**, 88 (2020).

[44] P. E. C. Ashby and J. P. Carbotte, Magneto-optical conductivity of Weyl semimetals, Phys. Rev. B **87**, 245131 (2013).

[45] P. E. C. Ashby and J. P. Carbotte, Chiral anomaly and optical absorption in Weyl semimetals, Phys. Rev. B **89**, 245121 (2014).

[46] A. B. Sushkov, J. B. Hofmann, G. S. Jenkins, J. Ishikawa, S. Nakatsuji, S. Das Sarma, and H. D. Drew, Optical evidence for a Weyl semimetal state in pyrochlore $Eu_2Ir_2O_7$, Phys. Rev. B **92**, 241108 (2015).

[47] R. Y. Chen, S. J. Zhang, J. A. Schneeloch, C. Zhang, Q. Li, G. D. Gu, and N. L. Wang, Optical spectroscopy study of the three-dimensional Dirac semimetal $ZrTe_5$, Phys. Rev. B **92**, 075107 (2015).

[48] B. Xu, Y. M. Dai, L. X. Zhao, K. Wang, R. Yang, W. Zhang, J. Y. Liu, H. Xiao, G. F. Chen, A. J. Taylor, D. A. Yarotski, R. P. Prasankumar, and X. G. Qiu, Optical spectroscopy of the Weyl semimetal TaAs, Phys. Rev. B **93**, 121110(R) (2016).

[49] R. Y. Chen, Z. G. Chen, X.-Y. Song, J. A. Schneeloch, G. D. Gu, F. Wang, and N. L. Wang, Magnetoinfrared spectroscopy of landau levels and zeeman splitting of three-dimensional massless Dirac fermions in $ZrTe_5$, Phys. Rev. Lett. **115**, 176404 (2015).

[50] S. Ahn, E. J. Mele, and H. Min, Optical conductivity of multi-Weyl semimetals, Phys. Rev. B **95**, 161112(R) (2017).

[51] Y. Sun and A.-M. Wang, Magneto-optical conductivity of double Weyl semimetals, Phys. Rev. B **96**, 085147 (2017).

[52] H. Hsu and L. E. Reichl, Selection rule for the optical absorption of graphene nanoribbons, Phys. Rev. B **76**, 045418 (2007).

[53] D. Prezzi, D. Varsano, A. Ruini, A. Marini, and E. Molinari, Optical properties of graphene nanoribbons: The role of many-body effects, Phys. Rev. B **77**, 041404(R) (2008).

[54] J. Liu, A. Wright, C. Zhang, and Z. Ma, Strong terahertz conductance of graphene nanoribbons under a magnetic field, Appl. Phys. Lett. **93**, 041106 (2008).

[55] A. R. Wright, J. C. Cao, and C. Zhang, Enhanced optical conductivity of bilayer graphene nanoribbons in the terahertz regime, Phys. Rev. Lett. **103**, 207401 (2009).

[56] Y.-R. Chen, Y. Xu, J. Wang, J.-F. Liu, and Z. Ma, Enhanced magneto-optical response due to the flat band in nanoribbons made from the α-T_3 lattice, Phys. Rev. B **99**, 045420 (2019).

[57] L. K. Shi and J. C. W. Song, Large optical conductivity of Dirac semimetal Fermi arc surface states, Phys. Rev. B **96**, 081410(R) (2017).

[58] Z. Wang, Y. Sun, X.-Q. Chen, C. Franchini, G. Xu, H. Weng, X. Dai, and Z. Fang, Dirac semimetal and topological phase transitions in A_3Bi (A = Na, K, Rb), Phys. Rev. B **85**, 195320 (2012).

[59] Z. Wang, H. Weng, Q. Wu, X. Dai, and Z. Fang, Three-dimensional Dirac semimetal and quantum transport in Cd_3As_2, Phys. Rev. B **88**, 125427 (2013).

[60] D. I. Pikulin, A. Chen, and M. Franz, Chiral anomaly from strain-induced gauge fields in Dirac and Weyl semimetals, Phys. Rev. X **6**, 041021 (2016).

[61] J. Cano, B. Bradlyn, Z. Wang, M. Hirschberger, N. P. Ong, and B. A. Bernevig, Chiral anomaly factory: Creating Weyl fermions with a magnetic field, Phys. Rev. B **95**, 161306(R) (2017).

[62] E. V. Gorbar, V. A. Miransky, I. A. Shovkovy, and P. O. Sukhachov, Dirac semimetals $A_3Bi(A$ = Na, K, Rb) as $\mathbb{Z}_2$ Weyl semimetals, Phys. Rev. B **91**, 121101(R) (2015).

[63] E. V. Gorbar, V. A. Miransky, I. A. Shovkovy, and P. O. Sukhachov, Surface Fermi arcs in $\mathbb{Z}_2$ Weyl semimetals A_3Bi (A = Na, K, Rb), Phys. Rev. B **91**, 235138 (2015).

[64] S.-Y. Xu, C. Liu, S. K. Kushwaha, R. Sankar, J. W. Krizan, I. Belopolski, M. Neupane, G. Bian, N. Alidoust, T.-R. Chang, H.-T. Jeng, C.-Y. Huang, W.-F. Tsai, H. Lin, P. P. Shibayev, F.-C. Chou, R. J. Cava, and M. Z. Hasan, Observation of Fermi arc surface states in a topological metal, Science **347**, 294 (2015).

[65] G. D. Mahan, *Many-Particle Physics* (Springer, Berlin, 2000).

[66] C.-Z. Li, L.-X. Wang, H. Liu, J. Wang, Z.-M. Liao, and D.-P. Yu, Giant negative magnetoresistance induced by the chiral anomaly in individual Cd_3As_2 nanowires, Nat. Commun. **6**, 10137 (2015).

[67] R. Okugawa and S. Murakami, Dispersion of fermi arcs in weyl semimetals and their evolutions to dirac cones, Phys. Rev. B **89**, 235315 (2014).

[68] M. Erementchouk and P. Mazumder, Weyl fermions in cylindrical wires, Phys. Rev. B **97**, 035429 (2018).

[69] E. Witten, Three lectures on topological phases of matter, Riv. Nuovo Cimento **39**, 313 (2016).